

Article

The Bottleneck in the Scalar Dissipation Rate Spectra: Dependence on the Schmidt Number

Paolo Orlandi 

Dipartimento di Ingegneria Meccanica e Aerospaziale, Università La Sapienza, Via Eudossiana 16, I-00184 Roma, Italy; paolo.orlandi@fondazione.uniroma1.it

Abstract: The mean dissipation rate of turbulent energy reaches a constant value at high Taylor–Reynolds numbers (R_λ). This value is associated with the well-scaling dissipation spectrum in Kolmogorov units, where the maximum corresponds to the bottleneck peak. Even the scalar dissipation rate at the high R_λ considered in the present direct numerical simulations attains a constant value as Sc increases. In this scenario, the maximum of the scalar dissipation spectra reaches its peak within the bottleneck, starting at $Sc > 0.5$. A qualitative explanation for the formation of the two bottlenecks is related to the blockage of energy transfer from large to small scales in the inertial ranges. Within the bottleneck, the self-similar, ribbon-like structures transition into the rod-like structures characteristic of the exponential decay range. Investigating the viscous dependence of the bottleneck’s amplitude may be aided by examining the evolution of a passive scalar. As Sc decreases, the scalar spectra undergo changes across the wave number k range. The bottleneck is dismantled, and at very low Sc values, the spectrum tends towards Batchelor’s theoretical prediction, diminishing proportionally to $k^{-17/3}$. To comprehend the flow structures responsible for the bottleneck, visualizations of $\theta \nabla^2 \theta$ and probability density functions at various Sc values are presented and compared with those of $u_i \nabla^2 u_i$. The numerical method employed for generating three-dimensional spectra and quantities such as energy and scalar variance dissipation in physical space must be accurate, particularly in resolving small scales. This paper additionally demonstrates that the second-order finite difference scheme conserving kinetic energy and scalar variance in the inviscid limit in viscous simulations accurately predicts the exponential decay range in one-dimensional and three-dimensional turbulent kinetic energy and scalar variance spectra.



Citation: Orlandi, P. The Bottleneck in the Scalar Dissipation Rate Spectra: Dependence on the Schmidt Number. *Fluids* **2024**, *9*, 285. <https://doi.org/10.3390/fluids9120285>

Academic Editors: Yonghua Yan, Yong Yang, Goodarz Ahmadi and Nilanjan Chakraborty

Received: 16 October 2024
Revised: 8 November 2024
Accepted: 29 November 2024
Published: 4 December 2024



Copyright: © 2024 by the author. Licensee MDPI, Basel, Switzerland. This article is an open access article distributed under the terms and conditions of the Creative Commons Attribution (CC BY) license (<https://creativecommons.org/licenses/by/4.0/>).

Keywords: passive scalar; turbulence; direct numerical simulation

1. Introduction

In a previous work by Orlandi and Pirozzoli [1], direct numerical simulations (DNS) of forced isotropic turbulence at a relatively high Taylor–Reynolds number, driving passive scalars at various values of Sc , were performed. This study follows the trend of previous simulations by Bogucki et al. [2], Wang et al. [3], Watanabe and Gotoh [4], Donzis et al. [5], Donzis et al. [6], and experiments by Dillon and Caldwell [7], and Oakey [8] that focused on values of $Sc > 0.5$. In Orlandi and Pirozzoli [1], the DNS results reported the formation of a k^{-1} spectrum range starting from $Sc = 2$, with its width increasing with the Sc number. This result was also predicted by Gibson [9], suggesting that the occurrence of the k^{-1} range does not need $Sc \gg 1$, based on the Batchelor [10] arguments. The other limit of scalar spectra for $Sc \ll 1$, arising from the theory of Batchelor et al. [11] and Gibson [9] leads to scalar spectra with a wide range of $k^{-17/3}$. All the ranges of Schmidt numbers have been investigated by DNS, whose exhaustive list is reported by Sreenivasan [12]. To better understand the formation of these ranges, it is worth analyzing the normalized scalar dissipation spectra (Bogucki et al. [2]). At high and intermediate values of Sc the maximum of scalar dissipation does not depend on Sc , with the peak at a normalized wave number equal to 0.25, consistent with the oceanic data by Oakey [8]. In previous studies

was not investigated at which value of $Sc < 1$ the collapse of the spectra ended, and this is one of the goals of the present research. The interest of the physics of passive scalar at $Sc \ll 1$ was less investigated due to few real applications that those at $Sc \gg 1$. The theoretical Batchelor’s prediction was confirmed by the DNS of Yeung and Sreenivasan [13]. At $Sc > 1$ the analysis of mixing is relevant in oceanography, in combustion and in many industrial applications. The $Sc < 1$ conditions are of interest, for instance, to have directions how to take into account the distortion of rays by the atmospheric turbulence on modern astronomical observations. In high speed flows in several conditions the mixing occurs in $Sc \ll 1$ conditions. In the present paper the DNS at $Sc < 1$ are used to understand how the spectra change with respect to the $Sc \approx 1$, in particular in the range of wave numbers before the peak of the scalar dissipation spectra.

The DNS results of Orlandi and Pirozzoli [1], focusing briefly on the differences between the bottleneck that occurs in the three-dimensional and one-dimensional energy and scalar spectra, support the conclusion of Dobler et al. [14], who argued that a strong bottleneck is observed only in numerical simulations in which three-dimensional spectra can be evaluated directly. In contrast, experimental spectra are generally derived from frequency spectra using the Taylor hypothesis, which explains why a clear spectral bottleneck is not deeply investigated. Orlandi and Pirozzoli [1] also observed that at $Sc > 0.5$ the amplitude of the bottleneck of the scalar spectra is larger than that of the energy spectra. The analysis was performed by evaluating quantities aligned with the principal axes of the strain field. The study shows that the enstrophy is primarily influenced by the vorticity, which is aligned with the intermediate principal strain axis, while the scalar gradient is mainly controlled by the compressive strain. This suggests that compressive strain plays a crucial role in determining the presence of the k^{-1} region in the scalar spectra within the bottleneck, supporting the absence of a k^{-1} region in the energy spectrum dominated by the vorticity structures aligned with the intermediate strain. In this work, we further our understanding of the complex physics by examining flow visualizations of $\frac{1}{Re} u_i \nabla^2 u_i$ and $\frac{1}{Pe} \theta \nabla^2 \theta$ at different Schmidt (Sc) numbers, where $Pe = Re \cdot Sc$ is the Péclet number. These two quantities, representing the rate of change in kinetic energy and scalar variance, can be locally positive or negative. However, their total contribution is negative, corresponding to the rates of energy and scalar dissipation. Notably, the positive contribution of $\frac{1}{Pe} \theta \nabla^2 \theta$ may vary with Sc , a behavior that has been analyzed through the Probability Density Function (PDF) of its fluctuating component and through flow visualizations in a plane.

2. Numerical Setup

The momentum and continuity equations for incompressible flows are as follows:

$$\frac{\partial u_i}{\partial t} + \frac{\partial u_i u_j}{\partial x_j} = -\frac{\partial p}{\partial x_i} + \frac{1}{Re} \frac{\partial^2 u_i}{\partial x_j \partial x_j} + F_i; \quad \frac{\partial u_j}{\partial x_j} = 0, \tag{1}$$

where u_i are the components of the velocity vector in the i directions, p is the pressure, x_1 , x_2 and x_3 are the three orthogonal space directions, and F_i is the external forcing to prevent decay of the turbulence kinetic energy $q = \langle u_i^2 \rangle / 2$. The passive scalar θ is transported by the velocity field, according to

$$\frac{\partial \theta}{\partial t} + \frac{\partial \theta u_j}{\partial x_j} = \frac{1}{ReSc} \frac{\partial^2 \theta}{\partial x_j \partial x_j} + F_\theta, \tag{2}$$

where F_θ is introduced to prevent the decay of the passive scalar variance, $\Theta = \langle \theta^2 \rangle / 2$. The numerical simulations are initiated with velocity and scalar fields with random phases, representing flows without structures but with high energy at low wave numbers and small energy at large wave numbers. The initial kinetic energy spectrum is given by the equation $E(k) = 64(k/8)^4 e^{-(k/8)} / 8$, with $q = \int E(k) = 1.5$ and $\int k^2 E(k) = 180$. The reference

velocity is $u_{\text{rms}} = 2q/3$, and the Taylor–Reynolds number (later defined) is related to the initial spectrum $E(k)$ through

$$Re = Re_0 \left(\frac{3}{20} \right)^{1/2} \frac{(2 \int k^2 E(k))^{1/2}}{\int E(k)}.$$

The value of Re is determined by assigning a value to Re_0 , as well as specifying the values of Sc . The same spectrum is used to generate the initial distribution of the passive scalar field Θ . The velocity components and the passive scalar in physical space are obtained using the method described by Rogallo [15].

The equations subjected to periodic boundary conditions are solved in the computational domain that is a cube of side 2π discretized by N uniform intervals. The finite difference scheme described in Orlandi [16] is summarized here. For the time integration, an implicit Crank–Nicholson scheme was used for the viscous terms, while a third-order Runge–Kutta scheme was employed for the convective terms. The staggered ordering of the velocity components by Harlow and Welch [17] effectively eliminated all odd decoupling phenomena, ensuring the discrete conservation of the total kinetic energy in the inviscid limit, as also confirmed and extended by Grammelvedt [18]. The dimensionless temperature θ was placed at the same location as u_2 , which is particularly advantageous in the presence of mean stratification, since it preserves the sum of potential and kinetic energy. In the Appendix A are reported the results demonstrating the conservation properties of energy and scalar variance. To facilitate the implementation of MPI (Message Passing Interface) coding, the computational domain was divided into layers parallel to the x_2 direction.

It is important to report what has been written in Orlandi and Pirozzoli [1] about forcing, since we believe that the differences between some of the global results on energy and passive scalar dissipation rate could be attributed to the type of forcing necessary to reach a statistical equilibrium state. Various forcing methods were discussed by Eswaran and Pope [19] based on the concept that at high Reynolds numbers the dynamics of the small scales should be decoupled from the large scales. However, manipulation of the large scales can affect the rate of energy dissipation. A statistical equilibrium state is reached when the dissipation rate oscillates around a constant value over time. Without forcing, the mean square velocity $q_i(t) = \langle u_i^2 \rangle = \int E_i(k, t) dk$ at any time has a total energy component $q_i(t) = \int E_i(k, t) dk$ smaller than the initial energy $q_i(0) = \int E_i(k, 0) dk$. By selecting a threshold wave number $|k|_F$, the energy $\delta q_i(t)$ within the range $|k| \leq |k|_F$ is evaluated to determine the quantity $F_i = (q_i(0) - q_i(t)) / \delta q_i(t)$, which represents the fraction of energy lost. By modifying the $\hat{u}_i(n)$ components for $|k| \leq |k|_F$ by $\hat{u}_i = \sqrt{F_i} \hat{u}_i(n)$, the total energy q_i can be kept constant over time. In the simulations described here, a numerical scheme in physical space is used so that three-dimensional FFT operations are used for the transition between physical and wave number space. Within the wave number space, the \hat{u}_i components are modified for $|k| \leq |k|_F$. Then, an inverse three-dimensional FFT is applied to obtain the modified velocity in physical space. To save computational time, forcing is applied only during the last of the three Runge–Kutta steps used for time progress. The same forcing approach is also used in solving the passive scalar transport equation, resulting in a constant $\Theta(t) = \int E_\theta(k, t) dk$ throughout the time evolution.

In contrast to the forcing scheme just described, Donzis et al. [6] used a forcing term for the scalar transport equation of the type $F_\theta = -u_i d\bar{\theta}/dx_i$, which mimics the action of a mean passive scalar gradient found in natural convection flows. They assumed a constant gradient $d\bar{\theta}/dx_i = 1$. In this scenario, not only does the rate of scalar dissipation vary with time, but also the magnitude $\Theta(t)$ is subject to time variations. Both forcing methods described by Eswaran and Pope [19] and Donzis et al. [6] were used in Orlandi and Pirozzoli [1]. Based on the results obtained, the present DNS was performed with a forcing that keeps the total energy and the total scalar variance constant.

3. Results

3.1. Scaling

The numerical simulations were performed at various Reynolds and Schmidt numbers, with the resolution chosen so that the maximum resolved wave number is $k_M^* \approx 1$, where the superscript * indicates the normalization in Kolmogorov units. The following definitions are needed to obtain this normalization from non-dimensional computational units:

$$\begin{aligned}
 u' &= \sqrt{\int 2Edk/3}, & D_v &= \int Ek^2dk, & \epsilon &= 2D_v/Re, & \eta &= (\epsilon Re^3)^{-1/4}, \\
 \lambda &= \sqrt{\frac{10 \int Edk}{\epsilon Re}}, & R_\lambda &= Re\lambda u', & S_E &= (\epsilon Re^5)^{-1/4}, & & (3) \\
 T' &= \sqrt{\int E_\theta dk}, & D_\theta &= \int E_\theta k^2 dk, & \chi &= \frac{2D_\theta}{ReSc^{3/2}}, & \eta_b &= \eta/\sqrt{Sc}
 \end{aligned}$$

These quantities have been evaluated through the three-dimensional energy $E = 0.5E_i$ and scalar variance E_θ spectra. As usual, ϵ and χ indicate the energy and scalar variance dissipation that are necessary to evaluate the Kolmogorov η and Batchelor η_b scales. The Taylor scale λ allows to obtain R_λ , usually used in isotropic turbulent flows. The energy spectra in Kolmogorov units are obtained by scaling the velocity spectra by S_E , which is the normalization factor for the energy. Similarly, the rms velocity is normalized by $S_U = S_E/\eta$. The scalar energy spectrum is scaled by $S_T = \frac{\chi\eta^{5/3}}{\epsilon^{1/3}}$, while the passive scalar rms value is normalized by $S_R = S_T/\eta_b$.

3.2. Global Flow Parameters and Validation

The objective of Donzis et al. [5]’s work was focused on the scalar dissipation rate. Therefore, the global results they reported were given to look at the trend of dissipation as a function of R_λ . Along with their results, they have published tables by other authors, e.g., Bogucki et al. [2], Wang et al. [3], Watanabe and Gotoh [4], and several experiments cited by Donzis et al. [5] with questionable data as discussed in Donzis et al. [5] and in Wang et al. [3]. The present data are reported in Table 1 in the same format as that of the tables in Donzis et al. [5].

One significant difference between our simulations and the findings reported in Donzis et al. [5] is that, in our setup, both u' and T' remain constant, whereas in their simulations, variations are observed. This choice has the consequence of reducing the variation in the quantities of our primary interest, namely, ϵ and χ . In Table 1 of Donzis et al. [5], the global results are reported at very low and moderately high values of R_λ , limiting the comparison to their results in a range of R_λ similar to our current study. Additionally, similar to the rate of dissipation, our present integral length scales also exhibit smaller variations compared to their data. Figure 1a illustrates the variations in the normalized energy dissipation rate versus R_λ in both numerical simulations, emphasizing a constant behavior in both cases. This observation aligns with previous investigations that suggest D_v increases with the Reynolds number, while ϵ remains constant, one of the fundamental concepts in the Kolmogorov theory. Furthermore, the behavior reported by Watanabe and Gotoh [4] indicates a constant value slightly smaller than ours, which may be attributed to differences in the forcing methodology. Another contributing factor may be related to the dealiasing procedure in the pseudospectral numerical method. As depicted in Figure 3 of Watanabe and Gotoh [4], the normalized energy dissipation spectrum at $k^* > 0.8$ exhibited a slight rise near the cutoff wave number, implying an inadequate resolution of the smallest scales. In contrast, our current numerical method yields an exponential decay at $k^* > 0.8$, as it is discussed later on. Our present simulations encompass the evolution of the passive scalar over a broad range of Sc numbers, spanning from 0.0025 to 6.5. It is crucial to emphasize that the highest value chosen can be viewed as a limiting threshold, as the normalized spectra do not largely change at higher values. This phenomenon was previously observed

in the DNS conducted by Orlandi and Pirozzoli [1], where they observed E_θ stabilizing around $(k_b^*)^{-1}$ starting at $Sc = 2$. At even higher Sc numbers, this range widens, aligning with the theoretical predictions made by Batchelor [10].

Table 1. The present global data in the same format as that in the table of Donzis et al. [5], with $L_u = \frac{\pi}{2u'^2} \int \frac{E}{k} dk$ and $L_T = \frac{\pi}{2T'^2} \int \frac{E_\theta}{k} dk$.

$R\lambda$	u'	L_u	ϵ	$\nu 10^3$	Sc	T'	L_T	χ	N
306.3	1.00	1.30	0.44	3.71	0.00250	1.73	1.37	2.26	768
313.5	1.00	1.30	0.42	3.71	0.01250	1.73	1.12	1.89	768
306.3	1.00	1.30	0.44	3.71	0.02500	1.73	1.14	1.54	768
313.5	1.00	1.30	0.42	3.71	0.12500	1.73	1.02	1.62	768
306.3	1.00	1.30	0.44	3.71	0.25000	1.73	0.98	1.63	768
306.3	1.00	1.30	0.44	3.71	0.50000	1.73	0.98	1.53	768
313.5	1.00	1.30	0.42	3.71	0.75000	1.73	0.93	1.68	768
313.5	1.00	1.30	0.42	3.71	1.00000	1.73	0.95	1.56	768
166.2	1.00	1.12	0.54	10.21	1.00000	1.73	0.88	1.83	1024
162.6	1.00	1.09	0.56	10.21	1.50000	1.73	0.89	1.63	1024
166.2	1.00	1.12	0.54	10.21	2.00000	1.73	0.95	1.58	1024
162.6	1.00	1.09	0.56	10.21	2.50000	1.73	0.81	1.75	1024
166.2	1.00	1.12	0.54	10.21	4.00000	1.73	0.86	1.60	1024
162.6	1.00	1.09	0.56	10.21	4.50000	1.73	0.83	1.61	1024
166.2	1.00	1.12	0.54	10.21	6.00000	1.73	0.84	1.58	1024
162.6	1.00	1.09	0.56	10.21	6.50000	1.73	0.84	1.57	1024
302.3	1.00	1.23	0.44	3.71	0.50000	1.73	0.91	1.70	1152
309.9	1.00	1.21	0.42	3.71	0.75000	1.73	0.93	1.70	1152
302.3	1.00	1.23	0.44	3.71	1.00000	1.73	0.84	1.69	1152
309.9	1.00	1.21	0.42	3.71	0.75000	1.73	0.93	1.70	1152
302.3	1.00	1.23	0.44	3.71	1.00000	1.73	0.84	1.69	1152
309.9	1.00	1.21	0.42	3.71	1.50000	1.73	0.99	1.46	1152
309.9	1.00	1.21	0.42	3.71	2.00000	1.73	0.81	1.76	1152
264.9	1.00	1.19	0.43	4.95	2.50000	1.73	0.86	1.64	1152
264.9	1.00	1.19	0.43	4.95	3.00000	1.73	0.85	1.63	1152
264.9	1.00	1.19	0.43	4.95	4.00000	1.73	0.84	1.62	1152

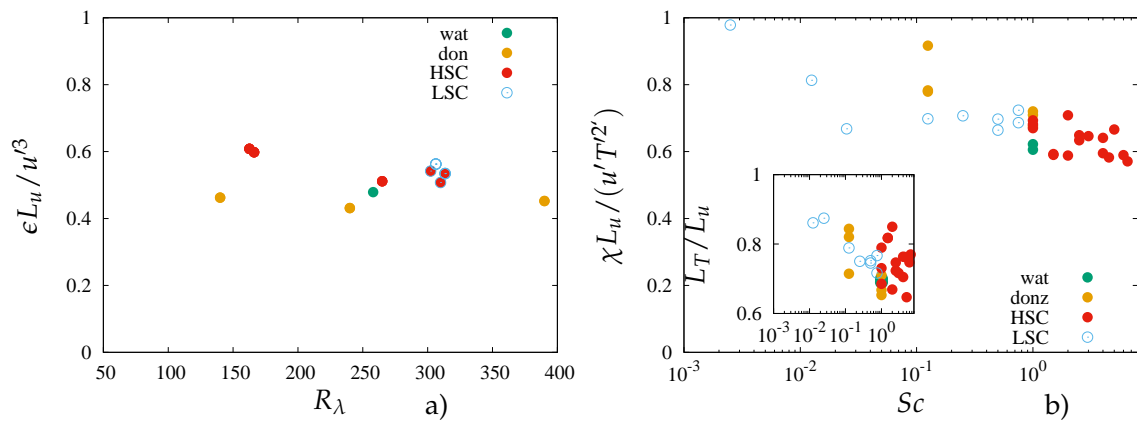


Figure 1. (a) Normalized energy dissipation rate versus R_λ ; (b) scalar dissipation rate normalized with L_u/u' in the inset of (b) L_T/L_u versus Sc ; present: red solid circle $Sc > 1$ indicated by HSC, blue open circle $Sc < 1$ indicated by LSC; green solid circle, Watanabe and Gotoh [4], orange solid circle, Donzis et al. [5].

In Figure 1b, we depict the scalar dissipation rate normalized by $\chi L_u / (u' T'^2)$ as a function of the Schmidt number. Notably, differences emerge when compared to the results of Watanabe and Gotoh [4] and Donzis et al. [5]. Across all the simulations considered, different values of $\chi L_u / (u' T'^2)$ are evident at the same Sc , indicating an influence of R_λ . Our present findings reveal a declining trend in the normalized scalar dissipation rate,

with a high probability of reaching a constant value, approximately equal to 0.6. The ratio L_T/L_u , despite some scattered data, decreases with increasing Sc , as illustrated in the inset of Figure 1b.

4. Dissipation Spectra: The Exponential Decay Range

The primary objective of this study is to investigate the formation of a bottleneck which, as emphasized by Dobler et al. [14], is more pronounced in three-dimensional energy and scalar spectra. Figure 2a demonstrates, at $R_\lambda = 310$, that in the compensated transverse one-dimensional spectra (green and black lines), the bottleneck is barely visible, and that it disappears in the longitudinal one. On the other hand, the bottleneck has a rather large amplitude in the three-dimensional spectra (red solid symbols). Figure 2b demonstrates that the amplitude and location of the bottleneck are independent of R_λ if all dissipative scales are resolved. The bottleneck forms only when the exponential decay range is reproduced, which is associated with the inhibition of energy transfer from large to small scales in the inertial range. The energy cascade in this range is driven by self-similar ribbon-like structures that transform into rod-like shapes at a viscosity-determined size within the exponential decay range. As a result, the bottleneck region scales well in Kolmogorov units.

As shown by Orlandi and Pirozzoli [1], in the dissipation spectra, the bottleneck exhibits a higher amplitude compared to the compensated energy spectra, allowing for a better sign of the dissipating flow structures. Figure 2b–d displays these spectra in semi-logarithmic plots, which are also suitable for examining the accuracy of the resolution of small scales. In Figure 2b, the black dashed line, which fits the present data, exhibits an exponential decay with a prefactor value of 4.4. The one-dimensional spectra measured by Saddoughi and Veeravalli [20] in an experiment conducted at very high Reynolds numbers found an exponential decay with a value of 5.2. To investigate whether the exponential decay rate for the three-dimensional spectrum differs from that of the one-dimensional spectra, semi-logarithmic plots of the present and of the Jiménez et al. [21] compensated one- and three-dimensional spectra indicate that the one-dimensional longitudinal and transverse spectra fit well an exponential decay with a prefactor equal to 5.2 in perfect agreement with Saddoughi and Veeravalli [20]. Moreover, the dissipation energy spectrum reported by Jiménez et al. [21] fits approximately $A \exp(-4.4k^*)$ with $A = 8$, while the results from Ishihara et al. [22] differ from both the present findings and those of Jiménez et al. [21]. This figure demonstrates that the present finite difference second-order numerical method does not introduce any numerical viscosity. Conversely, the pseudospectral method leads to an energy pile-up at the smallest scales. The dealiasing procedure may have a slight effect on the exponential decay range, as evidenced by comparing the trends of the two pseudospectral simulations.

In Figure 2c, the scalar dissipation spectra that Batchelor scaled at $Sc \geq 1$ show a notable collapse of the results that fit an exponential decay, similar to that of the energy dissipation spectra with a value $A = 12$ instead of $A = 8$. This collapse of the spectra is particularly pronounced for $k_b^* < 1$ and indicates that the maximum is reached at approximately $k_b^* \approx 0.25$, consistent with the oceanic spectra measurements by Oakey [8] and the data shown in Figure 3 of Watanabe and Gotoh [4]. Conversely, the results in Figure 2d at $Sc \leq 1$ reveal the significant impact of decreasing Sc numbers on the exponential decay range, as well as an effect on the low k_b^* which we will analyze in more detail later. This figure underscores that at $Sc = 0.0025$, the dissipation spectrum up to $k_b^* = 4$ fits rather well with the spectrum predicted by the Batchelor et al. [11] theory, with $(k_b^2 E_\theta)^* \approx k_b^{-11/3}$. Our present findings indicate a continuous trend towards this decay and a simultaneous reduction in the amplitude of the bottleneck, which we will delve into further in the next section.

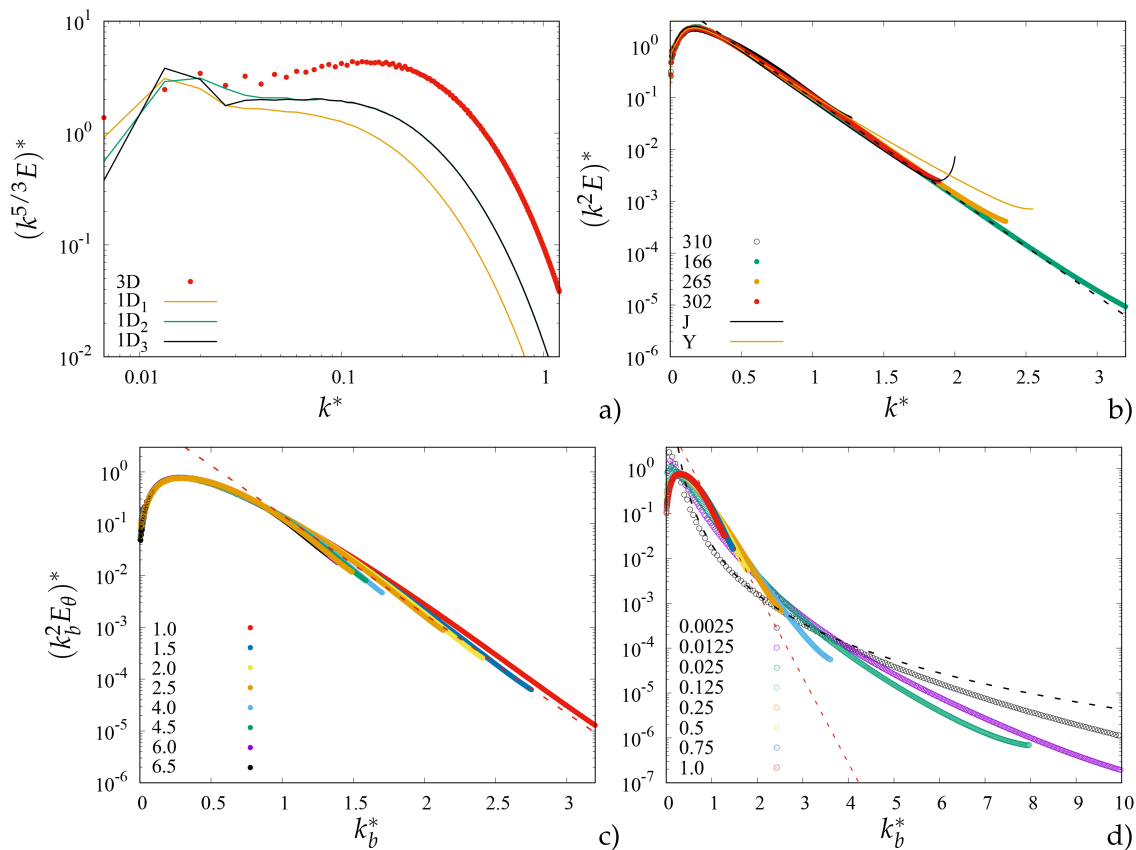


Figure 2. (a) Three- (red solid) and one-dimensional (lines) compensated energy spectra at $R_\lambda = 310$, with yellow longitudinal and green and black transverse; (b) energy dissipation rate compared with the DNS of the Jiménez et al. [21] black line and the Ishihara et al. [22] orange line; (c) scalar dissipation rate at high Sc ; (d) scalar dissipation rate at low Sc ; in (b), the black dashed line is $\approx 8.0e^{-4.4k^*}$, in (c), the red dashed line is $\approx 12.0e^{-4.4k_b^*}$, and in (d) the black line is $\approx 0.21k_b^{-11/3}$; the values of Sc are in the legend of (c,d), and the values of R_λ in the legend of (b).

5. The Bottleneck in the Energy and Scalar Variance Dissipation Spectra

The same dataset utilized to generate Figure 2 is also presented in Figure 3, where we employ the conventional log–log scales for spectral analysis. These log–log scales are typically used to examine spectra, and in the case of three-dimensional energy dissipation spectra, they help to emphasize the enstrophy-containing structures. These structures are the ones responsible for dissipating energy, contributing to the $\frac{1}{Re} u_i \nabla^2 u_i$ term in the turbulent energy transport equation. The same principle applies to the scalar variance transport equation, where dissipating scalar structures contribute to $\frac{1}{Pe} \theta \nabla^2 \theta$. These two quantities, which represent the rates of change in kinetic energy and scalar variance, can be locally positive or negative, although their total contribution is negative, corresponding to the rates of energy and scalar dissipation. Each term can be expressed for the velocity variance as $u_i \frac{\partial^2 u_i}{\partial x_i^2} = \frac{\partial^2 u_i^2}{\partial x_i^2} / 2 - (\frac{\partial u_i}{\partial x_i})^2$ and for the scalar variance as $\theta \frac{\partial^2 \theta}{\partial x_i^2} = \frac{\partial^2 \theta^2}{\partial x_i^2} / 2 - (\frac{\partial \theta}{\partial x_i})^2$. In homogeneous isotropic flows (Pope [23] pg. 132), the first term on the right-hand side has a zero total contribution, while the second term defined as pseudo-dissipation corresponds to the usual rate of energy dissipation: $\epsilon = 2\nu \langle s_{ij}s_{ji} \rangle = \nu \langle (\frac{\partial u_i}{\partial x_i})^2 \rangle = \nu \langle \omega_i \omega_i \rangle$, with s_{ij} the rate of strain tensor and ω_i the components of the vorticity vectors. For the scalar field, the second term gives the rate of scalar dissipation $\chi = \frac{1}{ReSc^{3/2}} \langle (\frac{\partial \theta}{\partial x_i})^2 \rangle$.

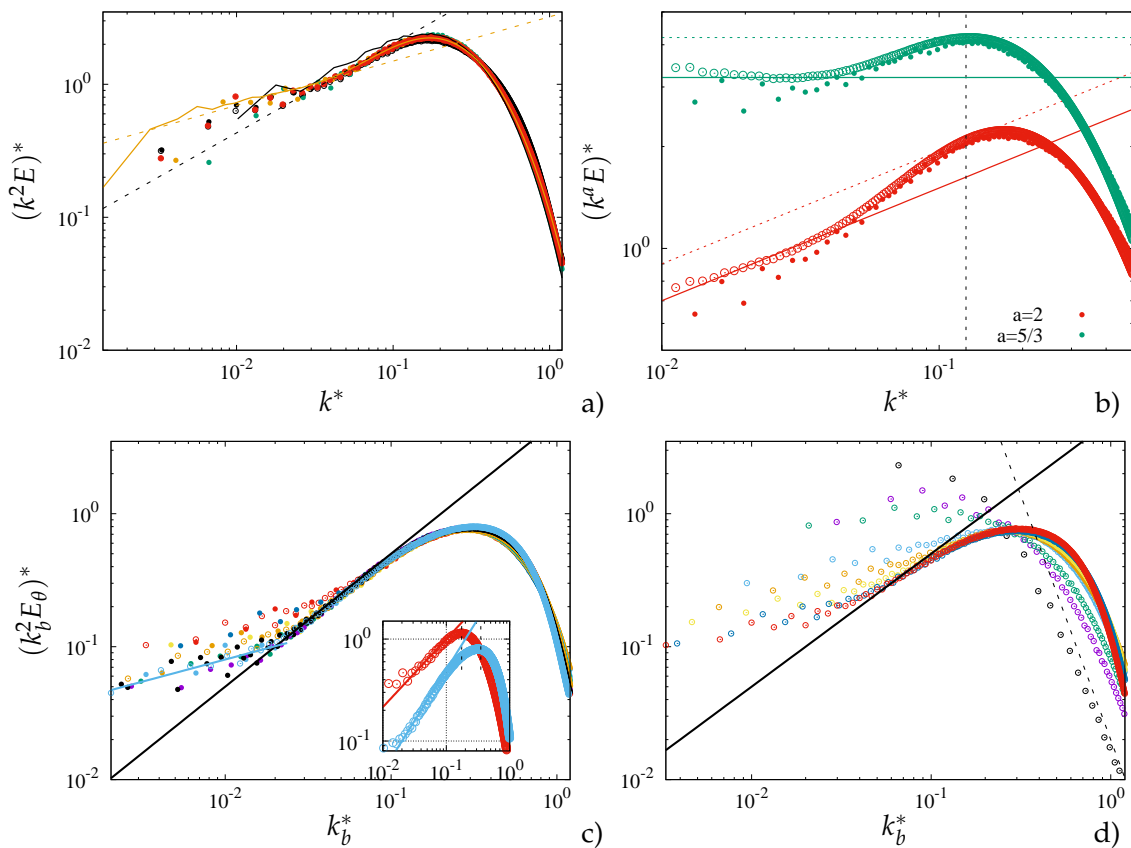


Figure 3. Spectra of (a) energy dissipation rate compared with the DNS of Jiménez et al. [21] (black line) and that by Ishihara et al. [22] (orange line). The black dashed line is $\approx k^{*2/3}$ and the orange one is $\approx k^{*1/3}$; in (b) are plotted the $(k^a E)^*$ $a = 2$ (red) and the $a = 5/3$ (green) by Ishihara et al. [22] (open circles) and for one of the present DNS (solid circles). The dotted fitting lines have values discussed in the text; (c) scalar dissipation rate at high Sc ; (d) scalar dissipation rate at low Sc ; in (c,d), the black solid line is $\approx k_b^*$; in (c), the blue solid line is $\approx k_b^{1/3}$; in (d), the black dashed line is $\approx 0.21 k_b^{-11/3}$; the values of Sc are in the legend of Figure 2 and in the inset of (c) are plotted the $(k^2 E)^*$ (red) and the $(k_b^2 E_\theta)^*$ at $Sc = 4$ (blue); the blue line is $0.5 k_b^*$, the red line is $4.64 k_b^{2/3}$, and the vertical dashed are at $k^* = 0.175$ and at $k_b^* = 0.35$.

As the Taylor R_λ number increases, the width of the inertial range in the energy spectra also widens, as demonstrated in Figure 3a through the comparison among our spectra, those of Jiménez et al. [21] at moderate R_λ and Ishihara et al. [22] at high R_λ . Notably, in Figure 3b, the compensated energy spectra in green $(k^{5/3} E(k))^*$ exhibit a flat slope in the inertial range, while the $(k^2 E(k))^*$ spectra in red have a $n = 1/3$ slope. Ishihara et al. [22] observed that their $(k^2 E(k))^*$ spectrum closely follows the orange dashed line ($3.25 k^{*1/3}$) over a wide range and touches the line $4.177 k^{*1/3}$ at $k^* = 0.125$, corresponding to the maximum of the bottleneck in the compensated energy spectrum $(k^{5/3} E(k))^*$. Figure 3b demonstrates that our spectra align quite well with the Ishihara et al. [22] spectrum. For the range $0.04 < k^* < 0.125$, the $(k^2 E(k))^*$ spectra in Figure 3a fit the black dashed line ($\approx k^{2/3}$), corresponding to $E^* \approx k^{-4/3}$. As indicated in Figure 2a, the $(k^2 E(k))^*$ spectra start to exhibit exponential decay for $0.4 < k^*$, which implies that the most significant contribution to energy dissipation comes from structures within the range of $0.03 < k^* < 0.45$. In the inset of Figure 3a, one of our spectra, along with the Ishihara et al. [22] spectrum, obtain $(k^2 E(k))^* > 1$ indicating the formation of a bottleneck in the spectrum. From the Ishihara et al. [22] spectrum, it has been inferred that within the range of $0.03 < k^* < 0.45$, these structures contribute to 10% of the total energy and to 72% of the total energy dissipation.

In Figure 3c, the normalized scalar dissipation three-dimensional spectra for $Sc \geq 1$ in Batchelor scales are superimposed on each other, particularly in the region of the bottleneck. For a significant portion of k_b^* , the spectra fit well with the black line represented by $5k_b^*$, which corresponds to a scalar spectrum $E_\theta^* \approx k_b^{*-1}$. It is worth noting that Watanabe and Gotoh [4] have shown in their Figure 3 that at $Sc = 1$ the compensated energy and scalar spectra have different shapes, with the energy spectrum peaking at $k^* = 1.5$ and the scalar spectrum peaking at $k^* = 2.0$. Additionally, they observed that the amplitude of the bottleneck is greater for E_θ^* than for E^* . Similar differences were discussed in Orlandi and Pirozzoli [1] by plotting the energy and scalar dissipation spectra. In the inset of Figure 3c, the $(k_b^2 E_\theta)^*$ and $(k^2 E)^*$ results for the DNS corresponding to that at $Sc = 4$ in Figure 2c are presented on a different scale. This clearly illustrates the distinct trends in the spectra beyond the short inertial range. Notably, for $0.03 < k_b^* < 0.9$, scalar dissipation contributes to 94% of the total, which is comparable to the energy dissipation evaluated by the Ishihara et al. [22] spectrum at high R_λ . The rightward shift of the k_b^* corresponding to the maximum of $(k_b^2 E_\theta)^*$ indicates that the scalar dissipation structures are smaller than the energy structures.

In Figure 3d, the normalized scalar dissipation three-dimensional spectra for $Sc \leq 1$ in Batchelor scales exhibit a notably different trend as the Schmidt number decreases. The well-defined k_b^{*-1} trend in Figure 3c becomes less visible. This absence is gradually accompanied by a reduction in the amplitude of the bottleneck, which disappears at $Sc = 0.125$. This transition occurs directly from the inertial range to the exponential decay range, as may be depicted by the profile of E_θ^* versus k_b^* . For $Sc < 0.125$, even the inertial range is disrupted, and E_θ^* decays at low wave numbers with a steeper slope than $n = 5/3$. This slope increases at higher wave numbers and eventually reaches at $Sc = 0.0025$, in agreement with the DNS by Yeung and Sreenivasan [13], the theoretical prediction by Batchelor et al. [11] for very low Sc , where $E_\theta^* \approx (k_b^{-17/3})^*$.

Three-dimensional spectra provide a representation of the distribution of energetic or dissipating scales. When appropriately normalized, these spectra reveal that the large-scale characteristics of energy and scalar fields are influenced by the Reynolds and Schmidt numbers. Conversely, for $Sc \geq 1$, the dissipating energy and scalar structures appear to be largely unaffected by changes in Re and Sc . However, in the case of scalar structures transported in flows with $Sc \leq 1$, their strength experiences a significant decrease. DNS enables the evaluation of various quantities, particularly the dissipating terms in the kinetic energy and scalar variance transport equations. Further insights into the spatial distributions of these terms are discussed in the following section.

6. Visualizations of the Dissipative Structures

The spectra presented in Figure 3 offer valuable insights into the changes in the rate of scalar dissipation concerning the Schmidt number. However, they do not provide an insight on the shape and on the spatial distribution of the structures contributing to the spectra bottlenecks in Figure 3c,d. When appropriately scaled, these structures appear independent of Sc at high Schmidt numbers (Figure 3c), suggesting a degree of physical similarity. Conversely, as Sc decreases, the bottleneck diminishes in amplitude and eventually disappears (Figure 3d), indicating changes in the scalar dissipation structures.

These structures are generated by a velocity field exhibiting a bottleneck in the spectrum due to the rate of kinetic energy dissipation, which is shifted to lower wave numbers compared to that of scalar dissipation, as shown in the inset of Figure 3c. Consequently, vortical and scalar gradient structures should exhibit distinct shapes. Among the various simulations discussed previously, four specific cases have been selected: the first two at $Sc = 1$ and $Sc = 4$ with $R_\lambda = 166.2$, representative of the cases in Figure 3c, and two at $Sc = 0.5$ and $Sc = 0.0025$ with $(k_b^2 E_\theta)^*$ spectra as in Figure 3d and $R_\lambda = 306.3$. For the case at $Sc = 4$, the $(k_b^2 E_\theta)^*$ spectrum in Figure 3c shows a short range with $(k_b^2 E_\theta)^* \approx k_b^{1/3}$ (short blue line) followed by a relatively long range with $(k_b^2 E_\theta)^* \approx k_b^1$ fitting the black line. In contrast, for the case at $Sc = 0.0025$, the $(k_b^2 E_\theta)^*$ spectrum exhibits a decay fitting the

$k_b^{-11/3}$ power law at high wave numbers (the black symbols in Figure 3d), differing from the exponential decay range at $Sc \approx 1$ (refer to Figure 2d).

From the values of $\mathcal{D}_v = \frac{1}{Re} u_i \nabla^2 u_i$ and $\mathcal{D}_\theta = \frac{1}{Pr} \theta \nabla^2 \theta$ in the entire computational domain and for a single realization, the mean values $\bar{\mathcal{D}}_v$ and $\bar{\mathcal{D}}_\theta$ are calculated. These mean values are then used to compute their fluctuating variables $D' = \frac{\mathcal{D} - \bar{\mathcal{D}}}{\langle (\mathcal{D}')^2 \rangle^{1/2}}$. Subsequently, these fluctuating values are used to determine their probability density functions (PDF) denoted as $p(D')$ and standardized moments ($\mu^n = \int (D')^n p(D') dD'$), with $\mu^2 = 1$. While the $\bar{\mathcal{D}}$ terms are typically negative and equal to $-\int k^2 E dk$, there may be several locations with positive \mathcal{D} , indicating a local generation of kinetic energy or scalar variance.

Table 2 provides data for the two simulations scrutinized in this section, including the values of $\bar{\mathcal{D}}$, the total negative contribution ($\frac{\langle \mathcal{D}^- \rangle}{\bar{\mathcal{D}}}$), $\langle (\mathcal{D}')^2 \rangle^{1/2}$, and the values of the μ^3 and μ^4 standardized moments. This table highlights that positive rate of change ($\frac{\langle \mathcal{D}^+ \rangle}{\bar{\mathcal{D}}} = \frac{\langle \mathcal{D}^- \rangle}{\bar{\mathcal{D}}} - 1$) for the kinetic energy is slightly smaller than that for scalar variance; the former increases with increasing R_λ , while the latter remains relatively constant for $Sc \geq 1$. Conversely, the $\frac{\langle \mathcal{D}^+ \rangle}{\bar{\mathcal{D}}}$ decreases as Sc decreases for $Sc \leq 0.025$. This outcome is closely related to the shape of small-scale energy-dissipating structures, which tend to be more rod-like compared to the scalar variance-dissipating structures influenced by the Schmidt number. In high Sc scenarios, these structures are thin and convoluted, as will be illustrated later through contours of $\mathcal{D}_\theta / \langle (\mathcal{D}'_\theta)^2 \rangle^{1/2}$ in a plane.

Table 2. Global quantities related to the rate of energy (the rows with u_i), and scalar variance dissipation (the rows with the value of Sc): the five rows on the top are related to the simulation at $R_\lambda = 166.2$, the others at $R_\lambda = 306.3$.

Case, Sc	$\bar{\mathcal{D}}$	$\frac{\langle \mathcal{D}^- \rangle}{\bar{\mathcal{D}}}$	$\langle \mathcal{D}'^2 \rangle^{1/2}$	μ^3	μ^4	$10\rho_{\mathcal{D}'_v, \mathcal{D}'_\theta}$
u_i	-0.330	1.493	1.177	-3.573	35.524	
1.000	-0.731	1.663	3.203	-3.401	33.858	0.0534
2.000	-0.577	1.796	2.899	-3.589	37.126	0.0875
4.000	-0.619	1.764	3.087	-3.593	36.812	0.2203
6.000	-0.581	1.727	3.079	-3.573	41.619	0.1370
u_i	-0.301	1.691	1.266	-3.046	31.359	
0.5000	-0.828	1.843	4.725	-3.889	44.702	0.0888
0.2500	-0.692	2.006	4.170	-3.001	38.300	-0.0073
0.0250	-0.842	1.795	3.861	-1.945	22.652	-0.1080
0.0025	-1.193	1.340	2.937	-1.551	8.594	-0.0188

The root mean square (rms) values of \mathcal{D}' and their higher moments in Table 2 indicate that, despite the significantly greater values of $\langle (\mathcal{D}'_\theta)^2 \rangle^{1/2}$ compared to $\langle (\mathcal{D}'_v)^2 \rangle^{1/2}$, the higher moments for the former are close to those for the latter. Furthermore, Table 2 emphasizes that these statistics are relatively independent of Sc for $Sc > 1$ and their values decrease as Sc decreases for $Sc < 1$. To give an explanation of these results, we will further explore the PDF of \mathcal{D}' , the joint PDF $J(\mathcal{D}'_v, \mathcal{D}'_\theta)$, and visualizations in a horizontal plane of $\frac{\mathcal{D}}{\langle (\mathcal{D}')^2 \rangle^{1/2}}$. We recognize the importance of using three-dimensional visualizations to distinguish rod-like or ribbon-like structures. Clear visual representations were provided by Orlandi and Pirozzoli [1], where the vorticity and scalar gradient components were projected onto the principal axes of the strain field. However, three-dimensional visualizations of \mathcal{D}' fail to convey the formation of adjacent positive and negative layers of \mathcal{D}'_θ at high Sc numbers and their disappearance at low Sc numbers.

The simulation at $R_\lambda = 166.2$ involved the transport of four scalars at $Sc = 1, 2, 4, 6$. Initially, a cursory examination of the PDF $p(\mathcal{D}'_\theta)$ suggests its independence from Sc , as shown by the superposition of the four $p(\mathcal{D}'_\theta)$ curves in Figure 4a. Minor differences are observed, particularly at high negative and positive values of \mathcal{D}'_θ . It is noteworthy that the distribution of $p(\mathcal{D}'_\theta)$ exhibits a highly negative skew, resembling the distribution of $p(\mathcal{D}'_v)$. The higher value of the $p(\mathcal{D}'_\theta)$ at $Sc = 6$ than those at the $Sc \geq 1$ may be related

to a insufficient resolution suggesting, how the visualizations are shown in Figure 4 at $Sc = 1$ and $Sc = 4$. The similar distribution of PDFs of D'_θ and D'_v may suggest a similarity between the structures corresponding to $\frac{D_v}{\langle (D'_v)^2 \rangle^{1/2}}$ and those of $\frac{D_\theta}{\langle (D'_\theta)^2 \rangle^{1/2}}$. Indeed, the visualizations show that these structures are different, and that the size of the scalar dissipating structures decrease by increasing the Sc number. Figure 4d clearly illustrates that the intense energy-dissipating structures exhibit, in certain locations, a rod-like shape, a phenomenon previously discussed by Orlandi and Pirozzoli [1]. This shape is attributed to the alignment of the vorticity vector with the intermediate principal axes strain component. The positive red contours, which have smaller amplitudes than the blue-coloured patches, are situated in close proximity to them. This suggests a diffusive contribution that is effectively balanced by the nearby negative contributions. Consequently, the total energy dissipation \overline{D}_v primarily stems from the contribution of the intense blue patches, which have a more rounded shape.

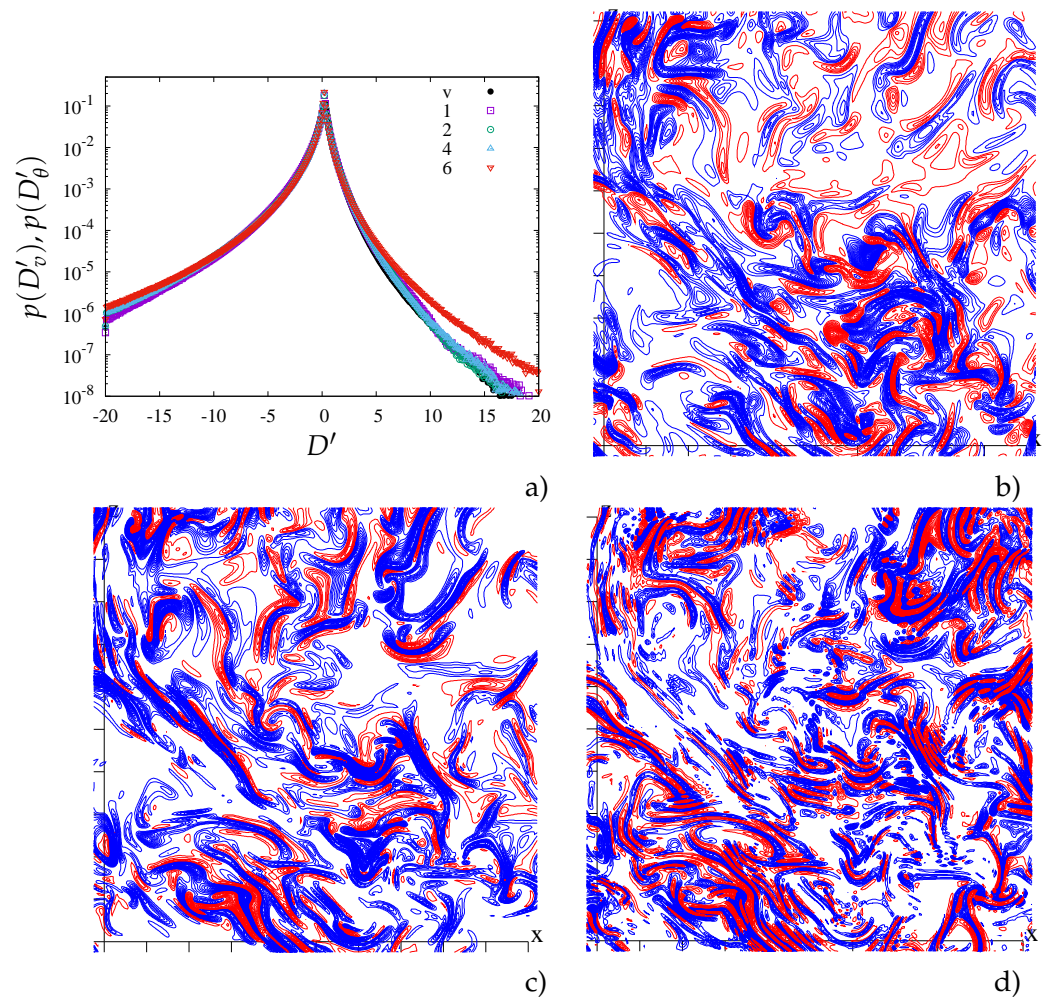


Figure 4. (a) PDF of D'_v (dashed lines) and D'_θ (open symbols) with the Sc numbers indicated in the labels; contour lines in $x - z$ planes for $-1 < x, z < 1$ at $y = 0$ in (b) of $\frac{D_v}{\langle (D'_v)^2 \rangle^{1/2}}$, in (c) of $\frac{D_\theta}{\langle (D'_\theta)^2 \rangle^{1/2}}$ at $Sc = 1$, and in (d) at $Sc = 4$, red is positive and blue is negative with increment $\Delta = 0.25$; the quadrant contributions to $\rho_{D'_v, D'_\theta}$ for $Sc = 1$ are 0.0799 for Q_I , -0.101 for Q_{II} , 0.111 for Q_{III} , and -0.0841 for Q_{IV} ; for $Sc = 4$ the contributions are 0.0730 for Q_I , -0.0822 for Q_{II} , 0.0955 for Q_{III} , and -0.0726 for Q_{IV} .

The correlation coefficients $\rho_{D'_v, D'_\theta}$ are evaluated by the $J(D'_v, D'_\theta)$, that, being similar, are not shown. The values of the correlation coefficients in Table 2 stress a weak correlation between the energy and scalar variance rate of change that cannot be gathered looking at

the visualizations in Figure 4. The Q_1 quadrants contribution obtained by the $J(D'_v, D'_\theta)$ given in the caption of Figure 4d leads to the establishment of a prevalence of the III positive on the II negative quadrants and a balance between the small contribution of the I and IV quadrants. A qualitative comparison of $\frac{D_\theta}{\langle (D'_\theta)^2 \rangle^{1/2}}$ at $Sc = 1$ in Figure 4c and at $Sc = 4$ in Figure 4d emphasizes that regions of intense scalar variance rate of change may be disconnected from those exhibiting a high rate of change in energy, as seen in Figure 4b.

Additional insights on the evolution and interaction of passive scalars with different diffusivity can be provided by evaluating correlation coefficients following the method described by Fox [24]. Preliminary evaluations of the correlation coefficients $\rho_{\alpha,\beta} = \frac{\langle \theta'_\alpha \theta'_\beta \rangle}{\sqrt{\langle (\theta'_\alpha)^2 \rangle \langle (\theta'_\beta)^2 \rangle}}$ between two scalars, one at $Sc = 1$ and the other at $Sc = 4$, yield $\rho_{1,4} \approx 0.5$. From the weak correlation between the two scalar variances and the even smaller values of $\rho_{D'_v, D'_\theta}$ in Table 2, it can be inferred that a passive scalar with a high Sc value has its own distinct time evolution. Consequently, in applications involving combustion or pollution, passive scalars with different diffusivities transported by a turbulent flow may have a low probability of interacting with each other.

For $Sc < 1$, the simulations were conducted at $R_\lambda = 302.3$. The probability density functions and the visualizations, similar to those presented in Figure 4, are provided in Figure 5. In these conditions, the PDFs of the energy rate of change in Figure 5a exhibit notable differences compared to the rate of change in scalar variance at $Sc < 0.5$ but align closely with those at $Sc = 0.5$. The subtle distinctions observed at the extremes of D' in Figure 5a account for the disparities between the third and fourth moments reported in Table 2. Figure 5c,d reveal significant disparities in the spatial distributions of the respective rates of change in scalar variance. Notably, $\frac{D_\theta}{\langle (D'_\theta)^2 \rangle^{1/2}}$ is small or nearly absent in regions characterized by strong $\frac{D_v}{\langle (D'_v)^2 \rangle^{1/2}}$ in Figure 5b. Even in this case at $Sc = 0.5$ in Figure 5d, the rate of change in scalar variance tends to concentrate within structures of a more convoluted nature compared to those associated with the rate of change in kinetic energy. However, both types of structures, thin and elongated, are primarily characterized by positive red values, which are counterbalanced by adjacent blue regions. The rather good correspondence of the white regions in Figure 5d with those in Figure 5c may suggest that the scalar correlation coefficient $\rho_{\alpha\beta}$, with α representing θ at $Sc = 0.5$ and β θ at $Sc = 0.0025$, is likely greater than that computed for $Sc = 1$ and $Sc = 4$. Indeed, a value of approximately $\rho_{0.5,0.0025} \approx 0.8$ has been determined. Even if the scalar variance correlations at $Sc < 1$ increase with respect to that at $Sc > 1$, the weak correlation between energy and scalar variance rate of change is stressed by the values of $\rho_{D'_v, D'_\theta}$ in Table 2. The quadrants contribution (in the caption of Figure 5) obtained by the $J(D'_v, D'_\theta)$ show that for $Sc < 1$ there is also a prevalence in the III positive on the II negative quadrants and a balance between the small contribution of the I and IV quadrants.

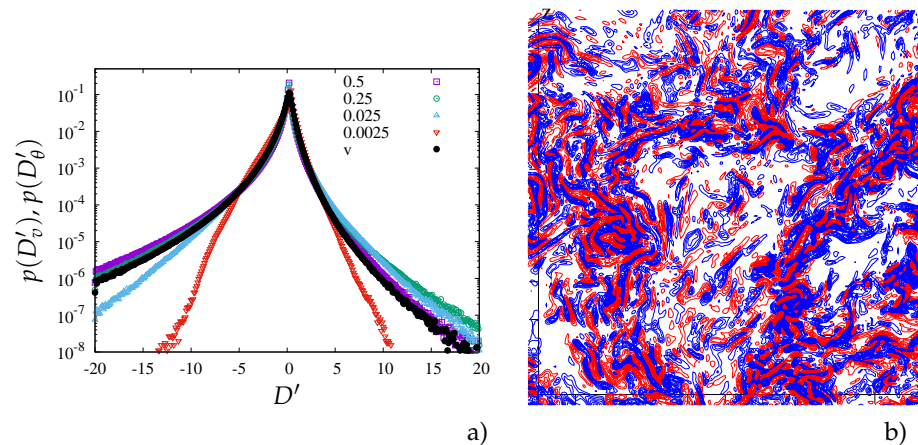


Figure 5. Cont.

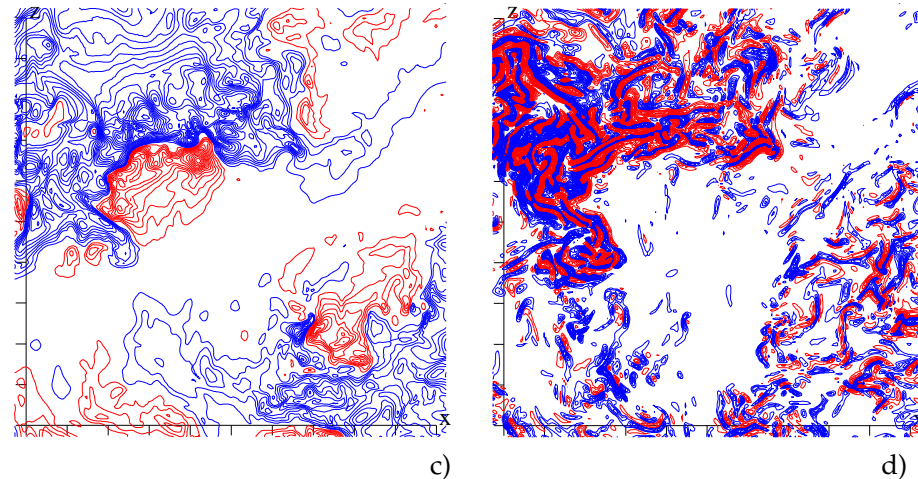


Figure 5. (a) PDF of D'_v (dashed lines) and D'_θ (open symbols) with the Sc numbers indicated in the labels; contours lines in $x - z$ planes for $-1 < x, z < 1$ at $y = 0$ in (b) of $\frac{D'_v}{\langle (D'_v)^2 \rangle^{1/2}}$, in (c) of $\frac{D'_\theta}{\langle (D'_\theta)^2 \rangle^{1/2}}$ at $Sc = 0.0025$, and in (d) at $Sc = 0.5$, with red being positive and blue being negative with increment $\Delta = 0.25$; the quadrants contributions to $\rho_{D'_v, D'_\theta}$ for $Sc = 0.0025$ are 0.0986 for Q_I , -0.123 for Q_{II} , 0.116 for Q_{III} , -0.0931 for Q_{IV} ; for $Sc = 0.5$ are 0.0719 for Q_I , -0.0853 for Q_{II} , 0.0945 for Q_{III} , -0.0721 for Q_{IV} .

7. Conclusions

The appearance of a bottleneck is more pronounced in three-dimensional spectra rather than one-dimensional spectra, which can be assessed through numerical simulations. The time evolution of three-dimensional spectra can be investigated by spectral closures like EDQNM (Eddy Dumped Quasi-Normal Markovian) [25] using a model to calculate the transfer term in the transport equation of the energy spectrum. In the energy spectra, the bottleneck forms at the end of the inertial range, signifying the conclusion of the energy cascade resulting from self-similar structures. [25] in the EDQNM closure demonstrated that in the inertial range, the triadic interaction entering in the transfer function is locally prevalent. The symmetry of the non-local interactions leads to an irrelevant contribution. At the end of the inertial range, the symmetry reduces and the non-local triadic interactions contribute to give the maximum of the transfer function in correspondence to the peak of the bottleneck. The simulation of two colliding dipoles by Orlandi et al. [26] allowed the investigation of the formation of three-dimensional spectra similar to those occurring in forced isotropic turbulence. Therefore, it was possible to see that at the end of the inertial range, the ribbon-like unstable structures evolve into the rod-like structures typically found in the exponential decay range. This scenario for kinetic energy remains unaltered at rather high Reynolds numbers and serves as the foundation for the Kolmogorov theory.

On the flip side, in the context of scalar variance, variations in the Schmidt number can result in the complete disruption of the bottleneck at specific values when $Sc \ll 1$. This disruption has been convincingly demonstrated in this study through the analysis of scalar variance dissipation spectra. Furthermore, it has been shown that when $Sc > 1$, the inertial range undergoes a transition towards exponential decay with different slopes depending on Sc , eventually converging toward the well-established k^{-1} range, as reported by Sreenivasan [12]. Whether $Sc \ll 1$ or $Sc \gg 1$, the dissipating scalar structures exhibit significant differences. However, the joint probability density function of the fluctuating change in energy and scalar variances is rather independent of the Sc number, establishing that they are not correlated.

Having established that numerical simulation is the most appropriate tool to generate three-dimensional spectra and quantities such as the changes in energy and scalar variance in physical space, it should be demonstrated that the numerical method used is accurate, particularly in resolving small scales. Typically, pseudospectral numerical methods are

employed, heavily relying on dealiasing procedures. This paper further demonstrates that a conservative second-order finite difference scheme predicts the correct behavior of the exponential decay range in one-dimensional and three-dimensional turbulent kinetic energy and scalar variance spectra. This understanding is crucial for advancing the knowledge of the complex physics governing the flow and scalar structures, which are responsible for the similarities and differences in the bottlenecks observed in the respective spectra.

In the direct numerical simulation (DNS) discussed in this paper, several scalars were transported by a single turbulent flow, providing a setup conducive to a more comprehensive exploration of differential diffusion in passive scalars, similarly to the study conducted by Yeung et al. [27]. Such research could be particularly relevant to combustion-related issues, where statistics derived from DNS can inform the development of models applicable at high Reynolds numbers. However, it is essential to clarify that this in-depth study lies beyond the scope of the present paper.

Funding: This research received no external funding.

Data Availability Statement: Dataset available on request from the authors.

Acknowledgments: A particular thanks is devoted to Sergio Pirozzoli for his comments on the first draft of this paper. The results reported in this paper have been achieved using the PRACE Research Infrastructure resource LUMIC.

Conflicts of Interest: The author declares no conflicts of interest.

Appendix A. Conservation Properties of the Numerical Method

The second-order finite difference scheme, with staggered velocity components located at the cell center, has been widely used in simulations of turbulent flows. However, several scholars still do not believe that the results from this method can be comparable to or even better than those obtained from pseudospectral simulations under certain conditions. A comparison of the present solver with fourth-order accurate schemes and pseudospectral methods was reported by Duponcheel et al. [28], demonstrating that in terms of energy conservation and time-reversibility, it produces results that are comparable to, and sometimes superior to, the other methods. The Taylor–Green vortex has often been used in inviscid simulations (Chichowlas and Brachet [29]) to investigate the occurrence of a finite time singularity (FTS) in the Euler equations. This initial condition concentrates kinetic energy at a single wave number, meaning that the evolution towards a turbulent state requires significant energy transfer from large to small scales before any considerable energy appears in the small-scale spectra. Theoretical considerations suggest that, near an FTS, the energy spectrum should develop an infinite k^{-3} range. In pseudospectral simulations, the dealiasing procedure often produces an energy pile-up followed by an exponential energy decay. However, such oscillations are not observed in finite difference spectra, allowing for the easier formation of a wide k^{-3} range.

In this work, the Taylor–Green vortex is used to demonstrate the conservation of kinetic energy and scalar variance in inviscid simulations as $\Delta t \rightarrow 0$. Unresolved simulations should lead to equipartition spectra characterized by a k^2 range at small scales. Two simulations were performed using the initial velocity distributions, u_1 and u_2 , from the Taylor–Green vortex in Chichowlas and Brachet [29], and a passive scalar distribution given by $\theta = |\omega_3|/\omega_{3,\max}$ (where ω_3 is the vorticity component). Figure A1a shows the evolution of errors, $e_v = 1 - q(t)/q_0$ and $e_\theta = 1 - \Theta(t)/\Theta(0)$, obtained from two coarse 128^3 simulations. One simulation uses a Courant–Friedrichs–Lewy (CFL) condition of $|U_i \Delta t / \Delta x_i| = 0.25$, while the other a value of 0.1. A significant reduction in errors for both energy and scalar variance is observed with a lower CFL condition. The evolution of energy and scalar spectra in Figure A1b shows that, at $t = 5$, the k^2 range at large k is not visible. Instead, a wide spectrum is present, with small-scale content being generated from large-scale structures. This behavior is nonphysical, but it highlights the necessity of the proper discretization of the nonlinear terms. A physical explanation why the error of

the turbulent energy is smaller than that for the scalar variance is linked to the difference discussed above, where the energy dissipating structures or the enstrophy are more rod-like while the scalar dissipating ones are ribbon-like.

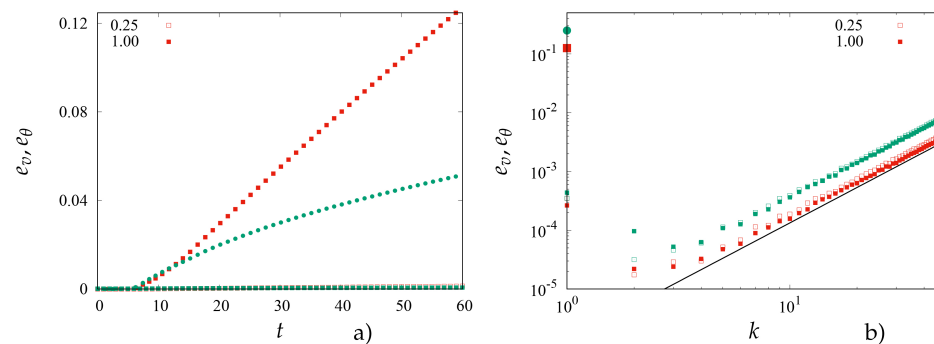


Figure A1. (a) Evolution of the errors e_v and e_θ in time open $CFL = 0.25$ solid symbols $CFL = 1$: red scalar, green kinetic energy; (b) energy and scalar spectra: closed symbols $t = 0$, green energy, and red scalar at $t = 60$; the black solid line is the theoretical k^2 equipartition distribution.

References

- Orlandi, P.; Pirozzoli, S. Effect of Schmidt number on forced isotropic turbulence with passive scalar. *Fluids* **2023**, *8*, 248. [\[CrossRef\]](#)
- Bogucki, D.; Domaradzki, J.; Yeung, P. Direct numerical simulations of passive scalars with $Pr > 1$ advected by turbulent flow. *J. Fluid Mech.* **1997**, *343*, 111–130. [\[CrossRef\]](#)
- Wang, L.; Chen, S.; Brasseur, J. Examination of hypotheses in the Kolmogorov refined turbulence theory through high-resolution simulations. Part 2. Passive scalar field. *J. Fluid Mech.* **1999**, *400*, 163–197. [\[CrossRef\]](#)
- Watanabe, T.; Gotoh, T. Statistics of passive scalar in homogeneous turbulence. *New J. Phys.* **2004**, *6*, 40. [\[CrossRef\]](#)
- Donzis, D.; Sreenivasan, K.; Yeung, P. Scalar dissipation rate and dissipative anomaly in isotropic turbulence. *J. Fluid Mech.* **2005**, *532*, 199–216. [\[CrossRef\]](#)
- Donzis, D.; Sreenivasan, K.; Yeung, P. The Batchelor Spectrum for Mixing of Passive Scalars in Isotropic Turbulence. *Flow Turbul. Combust.* **2010**, *85*, 549–566. [\[CrossRef\]](#)
- Dillon, T.; Caldwell, D. The Batchelor spectrum and dissipation in the upper ocean. *J. Geophys. Res. Ocean.* **1980**, *85*, 1910–1916. [\[CrossRef\]](#)
- Oakey, N. Determination of the rate of dissipation of turbulent energy from simultaneous temperature and velocity shear microstructure measurements. *J. Phys. Oceanogr.* **1982**, *12*, 256–271. [\[CrossRef\]](#)
- Gibson, C.H. Fine structure of scalar fields mixed by turbulence. II. Spectral theory. *Phys. Fluids* **1968**, *11*, 2316–2327. [\[CrossRef\]](#)
- Batchelor, G. Small-scale variation of convected quantities like temperature in turbulent fluid. General discussion and the case of small conductivity. *J. Fluid Mech.* **1959**, *5*, 113–133. [\[CrossRef\]](#)
- Batchelor, G.; Howels, I.; Townsend, A. Small scale variation of convected quantities like temperature in a turbulent fluid. Part.2 The case of large conductivity. *J. Fluid Mech.* **1959**, *5*, 134–139. [\[CrossRef\]](#)
- Sreenivasan, K.R. Turbulent mixing: A perspective. *Proc. Natl. Acad. Sci. USA* **2019**, *116*, 18175–18183. [\[CrossRef\]](#) [\[PubMed\]](#)
- Yeung, P.; Sreenivasan, K. Direct numerical simulation of turbulent mixing at very low Schmidt number with a uniform mean gradient. *Phys. Fluids* **2014**, *26*, 015107. [\[CrossRef\]](#)
- Dobler, W.; Haugen, N.E.L.; Yousef, T.A.; Brandenburg, A. Bottleneck effect in three-dimensional turbulence simulations. *Phys. Rev. E* **2003**, *68*, 026304. [\[CrossRef\]](#) [\[PubMed\]](#)
- Rogallo, R. *Numerical Experiments in Homogeneous Turbulence*; Technical Memorandum 81315; NASA: Washington, DC, USA, 1981.
- Orlandi, P. *Fluid Flow Phenomena—A Numerical Toolkit*; Kluwer Academic Publisher: Dordrecht, The Netherlands, 2000.
- Harlow, F.; Welch, J. Numerical Calculation of Time-Dependent Viscous Incompressible Flow of Fluid with Free Surface. *Phys. Fluids* **1965**, *8*, 2182–2189. [\[CrossRef\]](#)
- Grammelvedt, A. A survey of finite-difference schemes for the primitive equations for a barotropic fluid. *Mon. Weather. Rev.* **1969**, *97*, 384–404. [\[CrossRef\]](#)
- Eswaran, V.; Pope, S. An examination of forcing in direct numerical simulations of turbulence. *Comput. Fluids* **1988**, *16*, 257–278. [\[CrossRef\]](#)
- Saddoughi, S.; Veeravalli, S. Local isotropy in turbulent boundary layers at high Reynolds number. *J. Fluid Mech.* **1994**, *268*, 333–372. [\[CrossRef\]](#)
- Jiménez, J.; Wray, A.A.; Saffman, P.G.; Rogallo, R.S. The structure of intense vorticity in isotropic turbulence. *J. Fluid Mech.* **1993**, *255*, 65–90. [\[CrossRef\]](#)
- Ishihara, T.; Gotoh, T.; Kaneda, Y. Study of High Reynolds Number Isotropic Turbulence by Direct Numerical Simulation. *Annu. Rev. Fluid Mech.* **2008**, *41*, 165–180. [\[CrossRef\]](#)

23. Pope, S.B. *Turbulent Flows*; Cambridge University Press: Cambridge, UK, 2000.
24. Fox, R. The Lagrangian spectral relaxation model for differential diffusion in homogeneous turbulence. *Phys. Fluids* **1999**, *11*, 1550–1571. [[CrossRef](#)]
25. Crocco, L.; Orlandi, P. A transformation for the energy-transfer term in isotropic turbulence. *J. Fluid Mech.* **1985**, *161*, 405–424. [[CrossRef](#)]
26. Orlandi, P.; Pirozzoli, S.; Carnevale, G. Vortex events in Euler and Navier–Stokes simulations with smooth initial conditions. *J. Fluid Mech.* **2012**, *690*, 288–320. [[CrossRef](#)]
27. Yeung, P.; Sykes, M.; Vedula, P. Direct numerical simulation of differential diffusion with Schmidt numbers up to 4.0. *J. Fluid Mech.* **2000**, *12*, 1601–1604. [[CrossRef](#)]
28. Duponcheel, M.; Orlandi, P.; Winckelmans, G. Time-reversibility of the Euler equations as a benchmark for energy conserving schemes. *J. Comput. Phys.* **2008**, *227*, 8736–8752. [[CrossRef](#)]
29. Chichowlas, C.; Brachet, M. Evolution of complex singularities in Kida-Pelz and Taylor-Green inviscid flows. *Fluid Dyn. Res.* **2005**, *36*, 239–248. [[CrossRef](#)]

Disclaimer/Publisher’s Note: The statements, opinions and data contained in all publications are solely those of the individual author(s) and contributor(s) and not of MDPI and/or the editor(s). MDPI and/or the editor(s) disclaim responsibility for any injury to people or property resulting from any ideas, methods, instructions or products referred to in the content.